Article

Evaluation of the active targeting of melanin granules after intravenous injection of dendronized nanoparticles

Catalina Bordeianu, Audrey Parat, Sébastien Piant, Aurélie Walter, Christine Zbaraszczuk-Affolter, Florent Meyer, Sylvie Begin-Colin, Sébastien Boutry, Robert N. Muller, Elodie Jouberton, Jean-Michel Chezal, Bruno Labeille, Elisa Cinotti, Jean-Luc Perrot, Elisabeth Miot-Noirault, Sophie Laurent, and Delphine Felder-Flesch

Mol. Pharmaceutics, **Just Accepted Manuscript** • DOI: 10.1021/acs.molpharmaceut.7b00904 • Publication Date (Web): 04 Jan 2018

Evaluation of the active targeting of melanin granules after intravenous injection of dendronized nanoparticles

C. Bordeianu,[1,2] A. Parat, [1,2] S. Piant, [1,2] A. Walter,[1,2] C. Zbaraszczuk-Affolter,[3] F. Meyer,[3] S. Begin-Colin,[1,2] S. Boutry,[4,5] R. N. Muller, [4,5] E. Jouberton,[6,7] J.-M. Chezal, [6,7] B. Labeille, [8] E. Cinotti, [9] J.-L. Perrot,[8] E. Miot-Noirault,[6,7] S. Laurent,[4,5] D. Felder-Flesch[1,2]

[1] Université de Strasbourg, CNRS, Institut de Physique et Chimie des Matériaux de Strasbourg, UMR 7504, F-67000 Strasbourg, France. Delphine.Felder@ipcms.unistra.fr

[2] Fondation IcFRC/Université de Strasbourg, 8 allée Gaspard Monge BP 70028 F - 67083 Strasbourg Cedex.

[3] Université de Strasbourg, INSERM, UMR 1121 Biomatériaux et Bioingénierie, 11 rue Humann 67000 Strasbourg, France

[4] University of Mons, General, Organic and Biomedical Chemistry NMR and Molecular Imaging Laboratory, Avenue Maistriau 19, 7000 Mons, Belgium

[5] CMMI - Center for Microscopy and Molecular Imaging, MRI & Optical Imaging, Rue Adrienne Bolland 8, 6041 Gosselies, Belgium

[6] Clermont Université, Université d'Auvergne, Laboratoire d'Imagerie Moléculaire et Thérapie Vectorisée, BP 10448, F-63000 Clermont-Ferrand, France

[7] INSERM, U 1240, F-63005 Clermont-Ferrand, France

[8] CHU, Département de Dermatologie, 42000 St. Etienne, France

[9] Department of Medical, Surgical and Neurological Science, Dermatology Section, University of Siena, S. Maria alle Scotte Hospital, Siena, Italy

Abstract

The biodistribution of dendronized iron oxides, NPs10@D1_DOTAGA and melanin-targeting NPs10@D1_ICF_DOTAGA, was studied *in vivo* using MRI and planar scintigraphy through [^{177}Lu]Lu-radiolabeling. MRI experiments showed high contrast power of both dendronized nanoparticles (DPs) and hepatobiliary and urinary excretions. Little tumor uptake could be highlighted after intravenous injection probably as a consequence of the negatively charged DOTAGA-derivatized shell which reduces the diffusion across the cells' membrane. Planar scintigraphy images demonstrated a moderate specific tumor uptake of melanoma-targeted [^{177}Lu]Lu-NPs10@D1_ICF_DOTAGA at 2 h post intravenous injection, and the highest tumor uptake of the control probe [^{177}Lu]Lu-NPs10@D1_DOTAGA at 30min pi, probably due to the enhanced permeability and retention (EPR) effect. In addition, *ex vivo* Confocal microscopy

(EVCM) studies showed a high specific targeting of human melanoma samples impregnated with NPs10@D1_ICF_Alexa647_ DOTAGA.

Keywords: Iron oxides – Melanoma – Active targeting – Confocal microscopy – MRI - Dendrimers

1. Introduction

Cancer is a worldwide disease with high mortality, accounting for about 595,690 deaths, almost 1,620 people per day in 2016 according to the statistical analysis of American Cancer Society.[1] About 1,685,210 new cancer cases have been diagnosed in 2016. The 5-year relative survival rate for all cancers diagnosed in 2004 - 2010 was 68%, up from 49% in 1975–1977. The improvement in survival reflects both the earlier diagnosis of certain cancers and improvements in treatment. However, the number of people living beyond a cancer diagnosis reached nearly 14.5 million in 2014 and is expected to rise to almost 19 million by 2024.[2] Therefore, cancer diagnosis using advanced technologies is essential.

A major issue in current cancer research is the development of new targeted probes against critical cancer biomarkers for molecular imaging and/or targeted therapies that are capable of improving personalized diagnosis and treatment. Therefore, researchers have focused on innovative targeting strategies (monoclonal antibodies (MAb), fragments of MAb, small molecules, peptides) to address this problem with the goal of increasing selectivity and minimizing accumulation in healthy tissues.

In nanomedicine, active targeting, also called ligand-mediated targeting, involves utilizing affinity ligands on the nanomaterial' surface for specific retention and uptake by the targeted disease cells. To that end, ligands are selected to bind surface molecules or receptors overexpressed in diseased organs, tissues, cells or subcellular domains.[3] Therefore, the grafting of targeting ligands should increase cellular uptake of both drug and contrast agent, resulting in improved antitumor activity, reduced toxicity and increased target-to-background contrast during imaging, without altering the overall biodistribution.[4]

Antibodies were the first used targeting moieties due to their high specificity and wide availability.[5] Since then, other proteins, peptides, nucleic acid-based ligands and small molecules for specific targeting have been described.[6] Small molecular weight compounds have properties which strongly contrast from usual targeting ligands: small sizes and improved stability which translate into simple conjugation strategies and tunable nanomaterials' synthesis.[7]

The skin is the body's largest organ. Skin cancer begins in the epidermis, which is made up of two main types of cells which are the keratinocytes (roundish cells that give origin to all the different layers of the epidermis) and the melanocytes (cells that produce melanin and are found in the lower part of the epidermis).

Melanoma arises from the malignant transformation of melanocytes and is the fifth most common type of new cancer diagnosis in men and the seventh most common type in women.[8] If it is not diagnosed early, it is likely to invade nearby tissues and to spread widely to the other parts of the body.

Melanoma-associated antigens began to be defined and led to melanoma being among the first tumors to which monoclonal antibodies were produced. While the first treatments used to treat advanced-stage melanoma patients (i.e. Interferons (IFNs),[9] Interleukin (IL),[10] or Dacarbazine (DNA alkylating agent)[11]) led to disappointing results, recent innovative targeted and immuno-therapies such as Ipilimumab (CTLA-4 blockade),[12] Vemurafenib and Dabrafenib (anti-BRAF),[13] Cobimetinib and Trametinib (anti-MEK) and Pembrolizumab and Nivolumab (anti-PD-1) demonstrated regressions of metastatic disease and significant improvements in overall survival. Despite promising early results, these treatments are limited by their high relapse rates and undesired side-effects. Among the panel of therapeutic options, targeted radionuclide therapy (TRT) emerged as a potential tool to selectively treat disseminated forms of melanoma. In this context, radiolabeled ligands directed towards Melanocortin-1 (MC1) receptor or melanin-producing cells have been the most extensively studied.[14]

Radio-halogenated (Hetero)arylcarboxamide derivatives (ICF01102 [15]) targeting melanin-positive cells seem to be the most promising pigmented melanoma-seeking imaging agents in nuclear imaging,[16] while their radio-metallated (*e.g.* ^{99m}Tc) analogues have received little attention due to disappointing results such as compounds washing out from the tumor,

prominent uptake in non-target tissues (kidneys, liver) or rapid excretion of the probes.[17] ICF01012 [15] has already shown high, specific and long lasting binding to melanin *in vitro*. [18, 19] In 2015, we synthesized [^{111}In]In-radiolabeled ICF01012-dendritic nanoprobes showing tumor uptake values as high as 12.7 ± 1.6% ID.g^{-1} at 4 h post intravenous injection vs. 1.5 ± 0.5% ID.g^{-1} for the non-functionalized dendritic probe, and over 11% ID.g^{-1} for any tumor weight whatsoever. Considering the cooperative effect and active-targeting properties of those dendrimers, we hypothesized that ICF-decorated dendronized nanoparticles would also be optimal candidates as melanocytes targeting MRI probes. To confirm such hypothesis and be able to quantify specific tumor uptake, we synthesized multimodal [^{177}Lu]Lu-DOTAGA-dendronized IONPs bearing or not melanin-targeting ligands **(Scheme 1)** and assessed their *in vivo* targeting efficiency in melanoma B16 mice after intravenous injection. Those experiments were implemented by *in vitro* toxicological and internalization studies on B16-F1 cell line, by *in vitro* and *in vivo* MRI studies as well as by *ex vivo* confocal microscopy analyses.

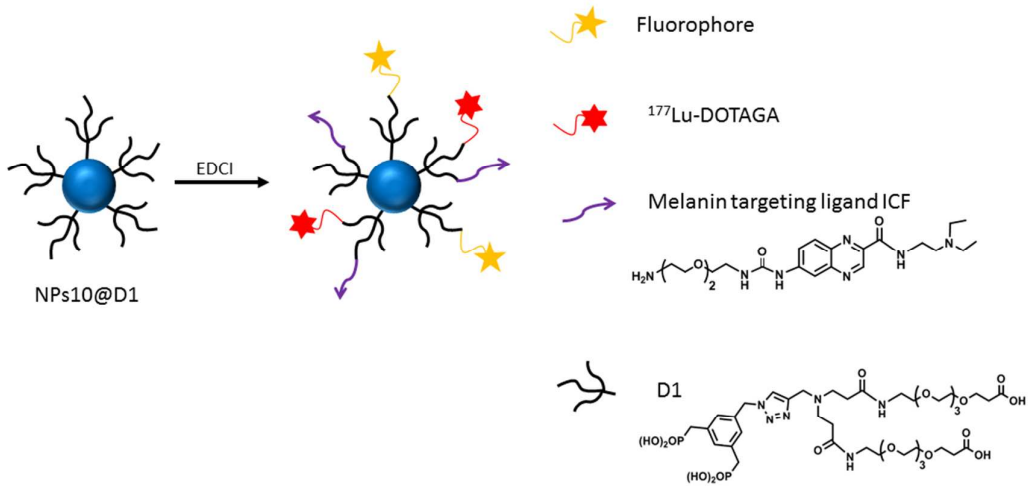

Scheme 1: Scheme of the dendronized iron oxide probes.

2. Materials and methods

Experimental procedures

The syntheses of organic coatings were performed under an argon atmosphere. The solvents (CH_2Cl_2, THF, ACN, DMF, MeOH, EtOH) were distilled or dried over 4 Å

molecular sieves. All commercially available reagents were used without further purification. Thin layer chromatography (TLC) analyses were performed on aluminum plates coated with Merck Silica gel 60 F254 and purifications by flash column chromatography were carried out using silica gel 60 and the specified eluent. Fourier transform infrared (FTIR) spectra were performed on Perkin Elmer and Digilab FTS 3000 spectrometer (samples were gently ground and diluted in non-absorbent KBr matrices) and are reported in reciprocal centimeters (cm^{-1}). The samples were compressed into KBr pellets. Matrix assisted laser desorption ionization time of flight (MALDI-TOF) mass spectra were acquired using a Bruker spectrometer. High resolution mass spectra were performed on Waters-QTOF spectrometer with electrospray ionization mode. Oligoethylene glycol (OEG) derivatives were purchased from Quanta BioDesign and used without further purification.

Nanoparticles characterization techniques

The NPs@OA, before and after grafting, were characterized by transmission electron microscopy (TEM) with a TOPCON 002B microscope operating at 200 kV, (point resolution 0.18 nm) and equipped with a GATAN GIF 200 electron imaging filter.

The grafting step was confirmed by Infra-Red spectroscopy using a Fourier Transform Infrared (FTIR) spectrometer (Digilab FTS 3000) (samples were gently ground and diluted in non-absorbent KBr matrices) and iron dosage by UV.

The colloidal stability of the aqueous suspensions was assessed by measuring the particle size distribution in water, at pH 7.4 and their zeta potential using a nano-size MALVERN (nano ZS) zetasizer.

Synthesis of 10 nm iron oxides by thermal decomposition and functionalization process

We previously published these procedures. Please see reference 21.

NPs10@D1_DOTAGA

To a suspension of 5 mg [Fe^{3+}] NPs@D1 in 5 mL H_2O at pH 6.5, 20 mg of EDCI were added at 0 °C. After 30 min mechanical stirring at 0 °C, 20 mg of NH_2DOTAGA [30] were added at 0 °C.

The suspension was mechanically stirred for 2h at room temperature. Once the grafting completed, ultrafiltration is performed, monitored by UV-Vis. Size measurement by DLS and zeta potential were performed on suspensions at pH 7.4.

NPs10@D1_ICF

To a suspension of 5 mg [Fe^{3+}] NPs@D1 in 5 mL H_2O at pH 6.5, 20 mg of EDCI were added at 0 °C. After 30 min of mechanical stirring at 0 °C, 15 mg of ICF[15] were added at 0 °C. The suspension was mechanically stirred for 2h at room temperature. Once the grafting completed, ultrafiltration is performed, monitored by UV-Vis. Size measurement by DLS and zeta potential were performed on suspensions at pH 7.4.

NPs10@D1_ICF_DOTAGA

To a suspension of 5 mg [Fe^{3+}] NPs@D1 in 5 mL H_2O at pH 6.5, 20 mg of EDCI were added at 0 °C. After 30 min mechanical stirring at 0 °C, 15 mg of ICF[15] were added at 0 °C. The suspension was mechanically stirred for one hour at room temperature. The suspension was cooled down to 0°C and 10mg of EDCI were added at 0°C. The mixture was mechanically stirred at 0°C for 30min, followed by addition of 15 mg of NH_2DOTAGA at room temperature for 2h. Once the grafting completed, ultrafiltration is performed, monitored by UV-Vis. Size measurement by DLS and zeta potential were performed on suspensions at pH 7.4.

NPs10@D1_Alexa495

To a suspension of 5 mg [Fe^{3+}] NPs@D1 in 5 mL H_2O at pH 6.5, 20 mg of EDCI were added at 0 °C. After 30 min of mechanical stirring at 0 °C, 0.25 mg of Alexa495 were added at 0 °C. The suspension was mechanically stirred for 2h at room temperature. Once the grafting completed, ultrafiltration is performed, monitored by UV-Vis. Size measurement by DLS and zeta potential were performed on suspensions at pH 7.4.

NPs10@D1_Alexa495_DOTAGA

To a suspension of 5 mg [Fe^{3+}] NPs@D1 in 5 mL H_2O at pH 6.5, 20 mg of EDCI were added at 0 °C. After 30 min mechanical stirring at 0 °C, 0.25mg of Alexa495 were added at 0 °C. The suspension was mechanically stirred for one hour at room temperature. Afterwards, the

suspension was cooled down to 0°C and 10mg of EDCI were added at 0°C. The mixture was mechanically stirred at 0°C for 30min, followed by addition of 20mg of NH_2DOTAGA at room temperature for 2h. Once the grafting completed, ultrafiltration is performed, monitored by UV-Vis. Size measurement by DLS and zeta potential were performed on suspensions at pH 7.4.

NPs10@D1_ICF_Alexa647_DOTAGA

To a suspension of 5 mg [Fe^{3+}] NPs@D1 in 5 mL H_2O at pH 6.5, 20 mg of EDCI were added at 0 °C. After 30 min mechanical stirring at room temperature, 15mg of ICF were added. The suspension was mechanically stirred for one hour. Afterwards, 10mg of EDCI were added and the suspension was mechanically stirred for 30min at room temperature. Following, 0.5mg of Alexa647 were added and the reaction was mechanically stirred at room temperature for 1 h. Then, 10mg of EDCI, 20mg of NH_2DOTAGA were added and the resulting suspension was mechanically stirred at room temperature for 2h. Once the grafting completed, ultrafiltration is performed, monitored by UV-Vis. Size measurement by DLS and zeta potential were performed on suspensions at pH 7.4.

Cells

Melanocyte mouse cell line B16-F1 (ATCC® CRL-6323™) was cultivated in DMEM supplemented with 10 % fetal bovine serum, 1 % penicillin /streptomycin solution and 0.3 mM L-tyrosine. Cells were sub-cultured at 1:10 before reaching confluence, usually at 80-90 % confluence, to avoid any melanin production. Melanin production was assessed spectrophotometrically at 405 nm. The detailed procedure for cells preparation can be found in reference 22.

MTT cytotoxicity assay

Cytotoxicity was evaluated by the MTT (3-[4,5-methylthiazol-2-yl]- 2,5-diphenyl-tetrazolium bromide) assay. In brief, B16-F1 cells (1 E 104 cells per well) were seeded in a 96-well plate and kept overnight for attachment. The next day the medium was replaced with fresh

medium with various concentrations of NPs1@D1_Alexa495 or NPs@D1_ICF_Alexa495 and cells were incubated for 24 h at 37 °C and 5% CO_2. Subsequently, the medium was discarded and cells were washed with 200 µL of Phosphate Buffer saline (PBS) in order to eliminate all remaining extracellular nanoparticles. 200 µL of cell culture medium + MTT (0.5 $mg.ml^{-1}$) was added to each well and cells were incubated for further 3h30 at 37 °C and 5% CO_2. After incubation, the medium was carefully discarded and 100 µl of DMSO was added to each well and stirred 15 min at room temperature under orbital shaking. The absorbtion of solubilized formazan crystals was measured at 550 nm using a Xenius microplate reader (SAFAS, Monaco).

Nanoparticles' cell internalization analysis

B16-F1 cells (105 cells per well) were seeded in a 12-well plate (Greiner, Dominique Dutscher, ref 165305) and kept overnight for attachment. The medium was replaced with either 1 mL of complete medium or 1 mL of complete medium supplemented with 50 nM of alpha-MSH. After three days of incubation at 37°C and 5 % CO_2, the medium was discarded, replaced with fresh medium containing nanoparticles, and cells were incubated for 24h at 37°C in 5% CO_2. Cells were thoroughly rinsed with 1 mL of cold PBS and then incubated with 300 µL of trypsin/EDTA solution (GIBCO, Ref R001100, Thermofisher) for 5 minutes. Cells were resuspended by the addition of 500 µL of PBS and harvested by centrifugation at 1000 rpm for 5 min. Cells were re-suspended in 1 mL PBS + 2% paraformaldehyde (PFA) and kept at 4°C protected from light until analysis. Cell' fluorescence was analyzed by flow cytometry using an FACScan flow cytometer with Novios software. Cells were analyzed in FL1 channel (Exc 488 nm, Em 505 nm). Fluorescence threshold was determined using none treated cells. 10 000 cells were analyzed by sample. Results are reported as the percentage of cell presenting fluorescence above the aforementioned fluorescence threshold.

In vivo MRI studies

In vivo experiments were performed on three C57BL6J mice bearingB16F0 murine melanoma xenografts. All experiments were performed 25 days post-cell inoculation when tumors were tangible (tumors of less than $1cm^3$). MRI coronal images were collected using a

BioSpec MRI at 11.7T, with a turbo-RARE factor of 4 and TE/TR = 12/2500ms. Twenty coronal slices, 1mm thick were acquired. For each slice, the field of view was 50 x 35 mm, with a 195 µM resolution in each orientation.

Radiolabelling

High purity [^{177}Lu]$LuCl_3$ [23] in diluted HCl (0.05 N) (2.5-3 µL, 114.8-129.2 MBq) was added in a glass vial containing a mixture of appropriate NPs10@D1_DOTAGA (0.3 mg) in water (400 µL) and Ammonium acetate buffer (0.2 M, pH 6, 400 µL). The vial was closed with a rubber stopper and sealed. The mixture was incubated for 45 min at 60 °C. After cooling down to room temperature, the reaction mixture was diluted to 3 mL with water and [177Lu]Lu-NPs10@D1_DOTAGA were separated from free [^{177}Lu]$LuCl_3$ by centrifugation through Amicon Ultracel 50 kDa (Merck Millipore) filters. To ensure that no radiochemical impurities would be present in the radiolabeled complex solution, which could have different biodistribution patterns rendering the investigations meaningless, radiochemical purity of the purified [^{177}Lu]Lu-NPs10@D1_DOTAGA was performed using silica gel plates impregnated glass fiber sheets (ITLC [24]-SG, Agilent Technologies) in aqueous 1 mM EDTA solution as the eluent. [^{177}Lu]Lu-NPs remained at the origin with a Rf value of 0, whereas residual [^{177}Lu]$LuCl_3$ migrated with a Rf of 1. The radiolabeled solution was stable prior to injection, presenting no aggregates, with a radiochemical purity as high as 96%. Radiochemical yields of 68-76% were obtained. At 15 h post labeling, a radiochemical purity decrease down to 90% was observed for [^{177}Lu]Lu-NPs10@D1_DOTAGA, which indicates that radiolabeled dendronized NPs10@D1_DOTAGA were kinetically stable over several hours thus suitable to perform *in vivo* quantitative biodistribution studies.

In vivo scintigraphy and biodistribution by ex vivo counting

The distribution of [^{177}Lu]Lu-NPs10@D1_DOTAGA or [^{177}Lu]Lu-NPs10@D1_ICF_DOTAGA was evaluated in eighteen B16F0 melanoma bearing mice by both *in vivo* planar scintigraphic imaging at 30 min, 2 h, 6 h and 24 h after administration (n = 2 to 3 animals/time point) and

by organ counting (protocol authorized by ethic committee as APAFIS #9355). Radiolabeled solutions were intravenously injected into the tail veins of mice at 4.3 ± 0.9 MBq for each animal. *In vivo* planar imaging was performed using a previously described protocol [25].

For biodistribution by organ counting, animals were sacrificed at 30 min, 2h, 6h and 24 h after administration of radioactive solution. Organs (tumor, eyes, heart, liver, stomach, kidneys, brain, spleen, intestines, muscle, bladder, lung, and bones) were removed, weighed and their radioactivity counted in the gamma-counter (Wizard, Perkin Elmer, France). After radioactive decay correction, the radioactivity in organs was expressed as the percentage of the total injected dose per gram of tissue (% ID/g).

Ex vivo Confocal Microscopy studies

Ex vivo Confocal Microscopy (EVCM) studies on human samples were performed at the biopsy of a dorsal Melanoma of a male patient. An elliptical excisional biopsy was performed and tumor samples of 4mm thickness were excised.

Fresh tissues were incubated with few drops of NPs10@D1 or NPs10@D1_ICF_Alexa647_ DOTAGA at Fe^{3+} concentration of 1.05mg/mL and 0.67mg/mL, respectively. Confocal images were acquired using a laser scanning reflectance and fluorescence confocal microscope Vivascope 2500®, (Caliber, New York, USA, distributed in Europe by MAVIG GmbH, München, Germany) with a wavelength of 830nm and 658nm for the reflectance and fluorescence mode, respectively. Analyses were performed at different incubation times and confocal mosaics were further processed with dark tones.

3. Results and discussion

We previously reported a complete library of functional dendritic phosphonic acids either fully PEGylated or derived from the poly(amido)amine (PAMAM) family.[26] The dendritic approach we presented consists in using dendritic architectures among which the suburb

and the nodal point can be functionalized and tuned. The PEG chain length, number or generation and the number of phosphonic anchors can be varied.

In this study, a PEGylated PAMAM dendron of generation 0.5 (D1) was synthesized (Scheme 1). The structure of this dendron may be easily modulated at the nanometric scale since it allows straightforward half-to-half generation growth.[27] PEG chains were introduced on the PAMAM dendron in order to prevent the DPs'opsonisation and to ensure water molecule capture and retention for improved MRI contrast enhancement. The strong contrast enhancement and the fast elimination of spherical iron oxides of 10 nm functionalized with D1 have been previously reported.[28]

NPs@OA (TEM images, see **Figure S1, ESI**) synthesized by thermal decomposition were functionalized with D1. Following purification step, the NPs' surface modification has been assessed by FTIR spectrometry **(Figure S2, ESI)**. [27] DLS and TEM analyses were performed on NPs10@D1 suspensions at pH = 7.4 in order to assess their colloidal stability and size distribution **(Figure 1)**.

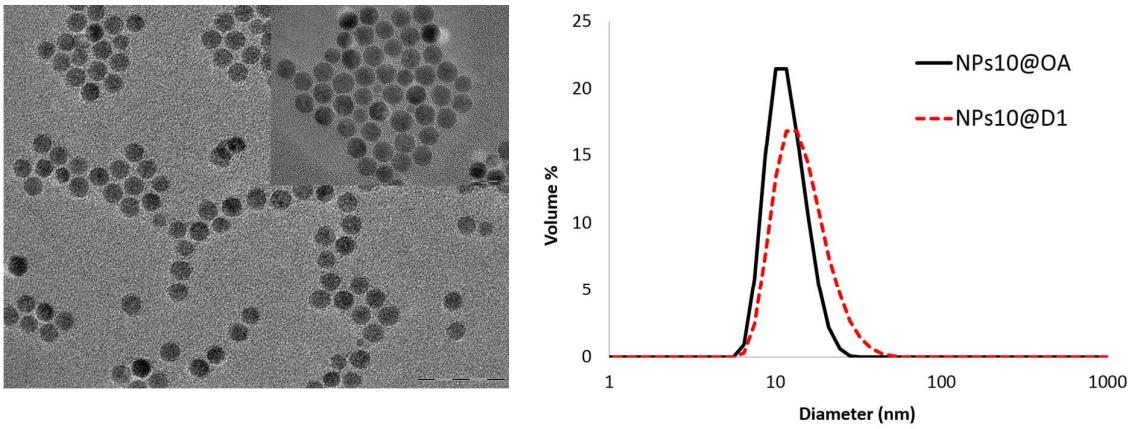

Figure 1: TEM images (left) of NPs10@D1 (insert: zoom) and size distribution (right) of NPs10@OA in THF and NPs10@D1 in water.

After ligand exchange, the particle size distribution of functionalized NPs10 suspension is monomodal (confirmed by TEM analysis **(Figure 1 left)**) with an average hydrodynamic diameter (16.8 nm) slightly larger than that of NPs@OA (12nm) **(Figure 1 right)** in agreement with the slightly longer size of the dendritic coating.

NPs10@D1 were further conjugated to 2,2',2''-(10-(4-((2-aminoethyl)amino)-1-carboxy-4-oxobutyl)-1,4,7,10-tetraazacyclododecane-1,4,7-triyl)triacetic acid (NH_2-DOTAGA [29])

through EDCI-mediated peptide coupling, for further labeling with ^{177}Lu radionuclide (Scheme 1).

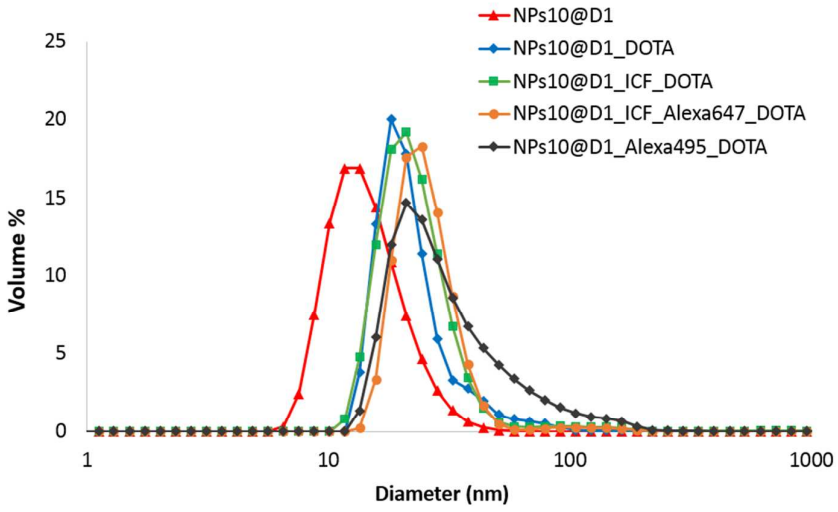

Figure 2: Size distribution evolution (by volume) of the different engineered nanoprobes.

For *in vivo* MRI and Scintigraphy studies, NPs10@D1_DOTAGA were used as a control for targeting nanoparticles NPs10@D1_ICF_DOTAGA. Also, Alexa-derived NPs such as NPs10@D1_Alexa495_DOTAGA (as control) and NPs10@D1_ICF_Alexa647_DOTAGA (as targeting probe) have been prepared to achieve *ex vivo* Confocal Microscopy (EVCM) studies (on previously *iv* injected mice but also on human excised melanomas).

Colloidal stability evaluated by DLS **(Figure 2)** and Zeta potential values assessed the functionalization of NPs10@D1 with the different molecules of interest (DOTAGA, targeting ligand ICF, Alexa647 and Alexa495) **(Table 1)**. The changes in the mean hydrodynamic size are in correlation with the added functionalities. Furthermore, Figure 2 shows the preservation of a monomodal size distribution throughout the addition of the different molecules on the NPs10@D1 periphery.

Table 1: Size distribution by volume, polydispersity index (PDI) and Zeta potential at pH = 7.4, before and after decoration of dendronized NPs10@D1 with the different molecules of interest.

	d^{DLS} (nm)	PDI	Zeta potential (mV)

NPs10@D1	16.8	0.14	-15.9
NPs10@D1_DOTAGA	19.8	0.19	-20.7
NPs10@D1_ICF_DOTAGA	29.6	0.43	-11
NPs10@D1_ICF_Alexa647_DOTAGA	35.4	0.51	-5.8
NPs10@D1_Alexa495_DOTAGA	27.3	0.37	-1.9

In vitro toxicity studies

In order to choose the optimal nanoparticle' concentration to be tested in internalization procedures without any cytotoxic effect, MTT cell viability assays were performed using increasing concentration of NPs10@D1_Alexa495 or NPs10@D1_ICF_Alexa495. As shown in **Figure 3**, both samples did not show any sign of cytotoxicity for concentrations up to 10mg/mL of Fe^{3+}. All internalization tests were then performed at such concentration.

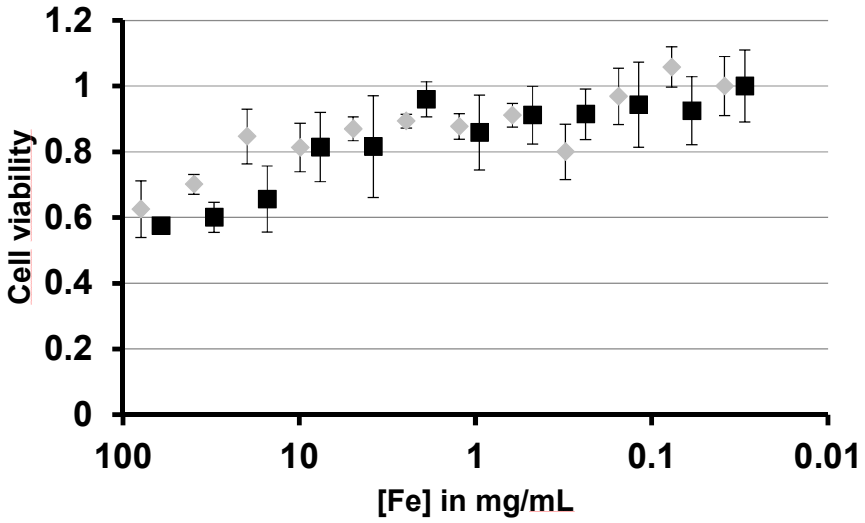

Figure 3: NPs10@D1_Alexa495 (grey diamond) and NPs10@D1_ICF_Alexa495 (black square) MTT cytotoxicity assay on B16-F1 cell line.

In vitro internalization studies

B16-F1 cells were chosen as cellular model as the production of melanin that is constitutive can be enhanced using alpha-MSH. Indeed, this peptide interacts with specific cytoplasmic

membrane receptor (MCR1) and triggers melanin synthesis. The NPs' internalization was tested on two specific cell populations: one population treated with 50 nM of alpha-MSH in order to enhance melanin production, and one untreated population showing a basal melanin synthesis (**Figure S3, ESI**). Internalization was assessed after 24 h incubation of B16-F1 cells with medium containing fluorescently labeled nanoparticles. Cells' fluorescence was analyzed by flow cytometry (**Figure 4**). As expected, NPs10@D1_Alexa495 bearing no targeting ligand showed a low internalization. Indeed the percentage of fluorescent cells which can be considered to have internalized nanoparticles is under 5 %. On the opposite, internalization of NPs10@D1_ICF_Alexa495 reached 15% showing the impact of the hydrophobic ligand ICF on the interaction with the phospholipids of the cellular membrane thus favoring internalization.

A difference in the percentage of positive cells (having internalized the fluorescent nanoparticles) was also observed between the two cell populations showing different levels of melanin production. Indeed, the cell population treated with alpha MSH showed a slightly better internalization compared to the untreated population, for both samples tested. As B16-F1 cells are constantly producing melanin, it is not surprising that an enhanced internalization was also observed for NPs10@D1_Alexa495. So far, further investigations are needed in order to precisely assess the internalization process.

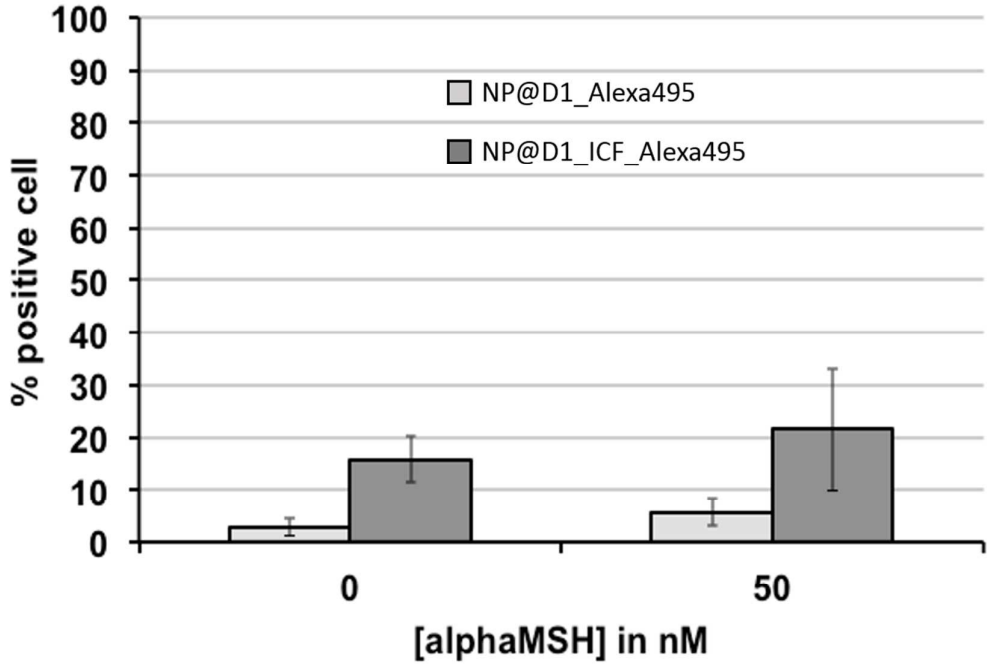

Figure 4: Flow cytometry analysis of B16-F1 cells incubated during 24h with either NPs10@D1_Alexa495 (light grey bar) or NPs10@D1_ICF_Alexa495 (dark grey bar).

In vitro MRI studies

Relaxation properties of NPs10@D1_DOTAGA and NPs10@D1_ICF_DOTAGA colloidal suspensions were studied in order to evaluate their possible use as MRI contrast agents (CAs). T_1 and T_2 values were measured over a concentration range of 1 to 230 µM and to 244 µM for NPs10@D1_DOTAGA and NPs@D1_ICF_DOTAGA respectively, diluted in doped water (1 µM $MnCl_2$). A solution of doped water was used as a control sample. Relaxometric rates ($1/T_1$ and $1/T_2$) were calculated and the results were plotted as a function of Fe^{3+} concentration **(Figure S4, ESI)**.

Longitudinal relaxivities (r_1) were found in the same range, and of 2.9 and 2.6 $mM^{-1}.s^{-1}$ for NPs10@D1_DOTAGA and NPs10@D1_ICF_DOTAGA respectively **(Table 2)**.

Table 2: *In vitro* relaxivity values of dendronized NPs compared to doped water, measured at 1.5T.

	R_1 (s^{-1})	R_2 (s^{-1})	r_1 ($mM^{-1}.s^{-1}$)	r_2 ($mM^{-1}.s^{-1}$)	r_2/r_1
Doped water	0.55	5	N/A	N/A	N/A
NPs10@D1_DOTAGA ([Fe^{3+}]=230µM)	0.68	38.5	2.9	144.5	49.8
NPs10@D1_ICF_DOTAGA ([Fe^{3+}]=244µM)	0.64	31.7	2.6	99.3	38.2

Transverse relaxation rates (r_2) vary considerably between NPs10@D1_DOTAGA and NPs10@D1_ICF_DOTAGA. Indeed, if an r_2 relaxivity value as high as 144.5 $mM^{-1}\cdot s^{-1}$ was obtained for NPs10@D1_DOTAGA, it lowered down to 99.3 $mM^{-1}\cdot s^{-1}$ for NPs10@D1_ICF_DOTAGA (Table 2). Consequently, grafting of ICF targeting ligand at the dendronized NPs' periphery caused an r_2 relaxivity decrease of about 30% which can be attributed to the ligand hydrophobicity, thus precluding water molecules to circulate freely close to the magnetic core.

The contrast enhancement properties of NPs10@D1_DOTAGA and NPs10@D1_ICF_DOTAGA were evaluated. Enhancement contrast ratios (EHC) were extracted from T_{2w} images (TR = 10,000ms) and calculated according to **Equation 1**, where S_{NPs}= signal value of DPs at each Fe^{3+} concentration and S_{water}= signal value of water:

Equation 1 $EHC\ \% = [(S_{NPs} - S_{Water})/S_{Water})] \times 100\%$

The high EHC values obtained for both dendronized NPs confirmed their great contrast power **(Figure S5, ESI)**. High iron concentrations led to signal loss for both dendronized NPs. Higher signal dropouts were noticed for NPs10@D1_ICF_DOTAGA compared to NPs10@D1_DOTAGA even at low iron concentrations.

For an echo time compatible with *in vivo* experiments, TE/TR = 100/2000ms parameters were used and image acquisition was both T_1 and T_2-weighted. **Figure 5 left** shows ghost images as a function of iron concentrations for NPs10@D1_DOTAGA. For the highest iron concentration, 0.23 mM, EHC % as high as 96% was obtained. One must also notice a slight positive contrast at the lowest iron concentrations (1 to 10 μm) **(Figure 5 right)**. Even if ICF-ligand grafting at the dendronized NPs' periphery induced a 30% decrease in r_2 relaxivity *in vitro*, those dendronized NPs10@D1_ICF_DOTAGA still show an important r_2 value, and high enough for *in vivo* investigations. These interesting properties might be related to the design of the dendronized NPs, which permits both preservation of the NPs magnetic properties and the minimization of the organic shell thickness necessary for a good water diffusion around the magnetic core and thus higher MRI responses.

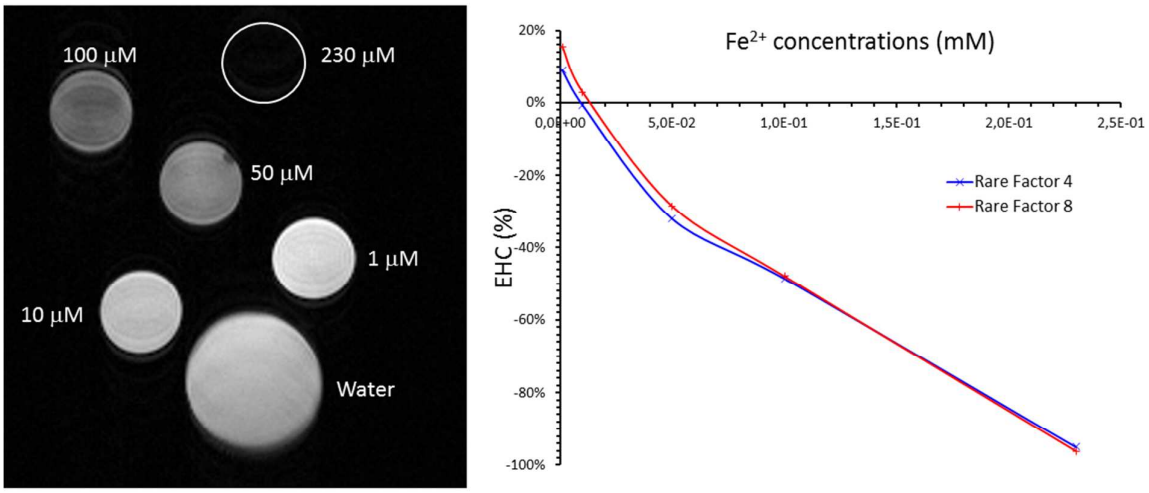

Figure 5: Left: Ghost images of NPs10@D1_DOTAGA at different iron concentrations, obtained in 100 s with a RARE factor of 8 and TE/TR = 100/200 ms. Right: EHC evolution according to two RARE factors.

In vivo MRI studies

Before administration of the contrast agent, a T_2-weighted 2-D MRI spin echo scan was performed and coronal images of the animal were acquired **(Figure 6, top)**.

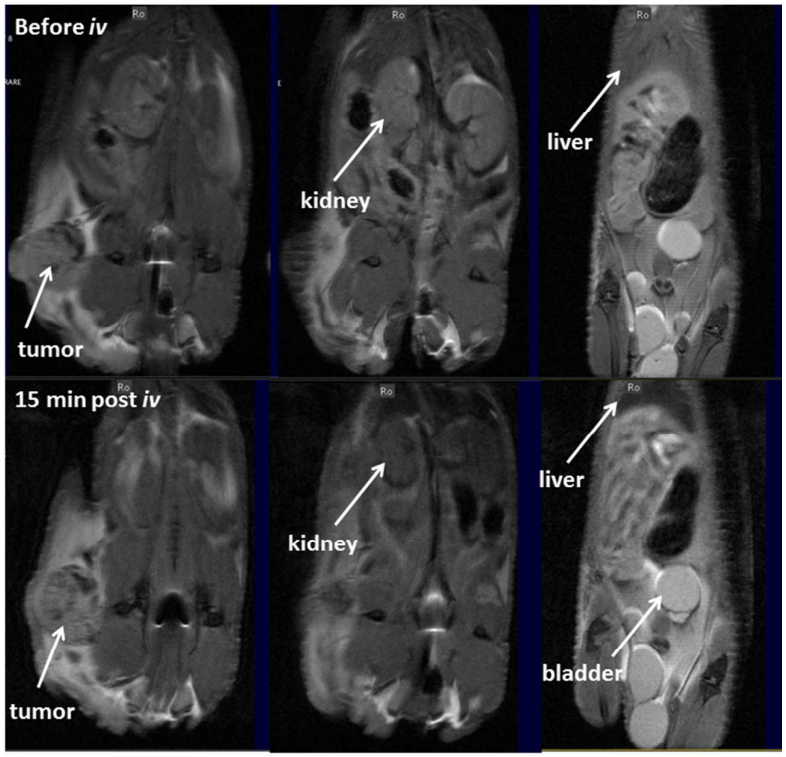

Figure 6: MRI images with a turbo-rare sequence of NPs10@D1_ICF_DOTA injected mouse at t = 0 (top) and 15 min (bottom) post intravenous (*iv*) injection (left and center: coronal incidence; right: sagittal incidence).

Then, the mice were intravenously injected with 200µL of NPs10@D1_ICF_DOTA at 12.2 mM, which corresponds to a 45 µmol [Fe^{3+}]/kg body weight dose. Coronal and sagittal images are represented in **Figure 6** for slices corresponding to different regions of interest (ROIs): tumor, kidneys, liver and urinary bladder. At 15 min following the injection, NPs10@D1_ICF_DOTAGA particles provided a clear and immediate liver signal decrease effect, on the contrary, low tumor uptake of dendronized NPs and no signs of urinary elimination have been noticed, which can be due to the short acquisition time post *iv* injection.

Furthermore, recorded EHC % of each ROI (kidneys, liver, tumor and muscle) allowed to compare the MRI signal as a function of the injected NPs' concentration and to follow the biodistribution processes over a longer period of time (100 min) after *iv* injection. Injections have been made with either 100 µL of NP@D1_ICF_DOTAGA at low (6.1 mM) and high (12.2 mM) Fe^{3+} concentration or with 200 µL at 12.2 mM Fe^{3+} concentration **(Figure 7)**. EHC were calculated according to **Equation 2**, where S_{biv}= signal value of the ROI before *iv* injection and S_{aiv}= signal value of the same ROI after *iv* injection:

Equation 2 $$EHC\ \% = [(S_{aiv} - S_{biv})/S_{biv}] \times 100\%$$

After injection of 12.2 mM NPs10@D1_ICF_DOTAGA for both volumes, a high negative contrast enhancement was observed in the liver (from -40 to - 60% at 15 min post-*iv*), and also in the kidneys (around -40% at 5 to 10 min post-*iv*) with a maximum at 20 min post injection; in the muscle and tumor, the obtained EHC values were of around -20% and relatively stable over time for injections of 200 µL at 12.2 mM. Furthermore, for 12.2 mM dose injections at different volumes, the decrease of EHC over time in liver and kidneys points out the potential hepatobiliary and urinary eliminations after a short period of time post *iv* injection.

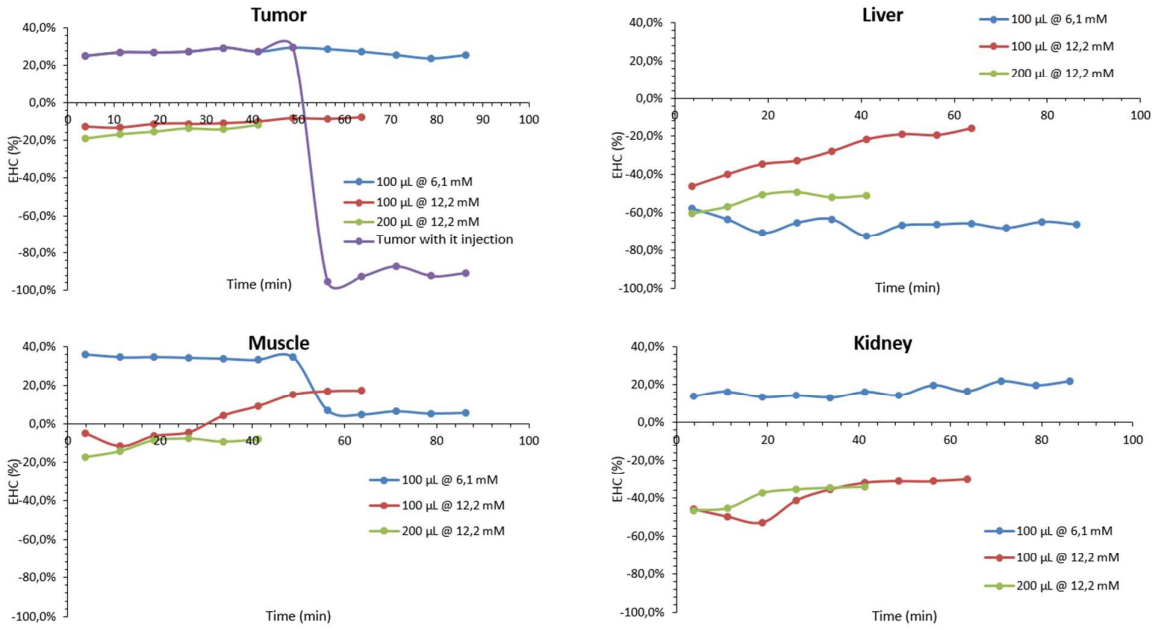

Figure 7: Calculated EHC % for different ROIs over time after intravenous injection of NPs10@D1_ICF_DOTAGA at various Fe^{3+} concentrations and for different injected volumes.

EHC values for low concentration dose of NPs10@D1_ICF_DOTAGA (100µL at 6.1 mM) show maximum uptake by the liver at 20 min post *iv* and negative contrast enhancement for muscle over 40 min, and for kidneys or tumor over 80 min.

In order to assess contrast induced in the tumor by NPs10@D1_ICF_DOTAGA, direct intratumoral (*it*) injection of 100 µL at 6.1 mM was investigated and the MR images were recorded over 50 min post-*it* **(Figure 8)**. Recorded EHC values in the tumor (Figure 7) show a maximum of -100% at *it* injection time and the slight evolution of the contrast enhancement over 50 min confirms no leakage of NPs10@D1_ICF_DOTAGA outside the tumor.

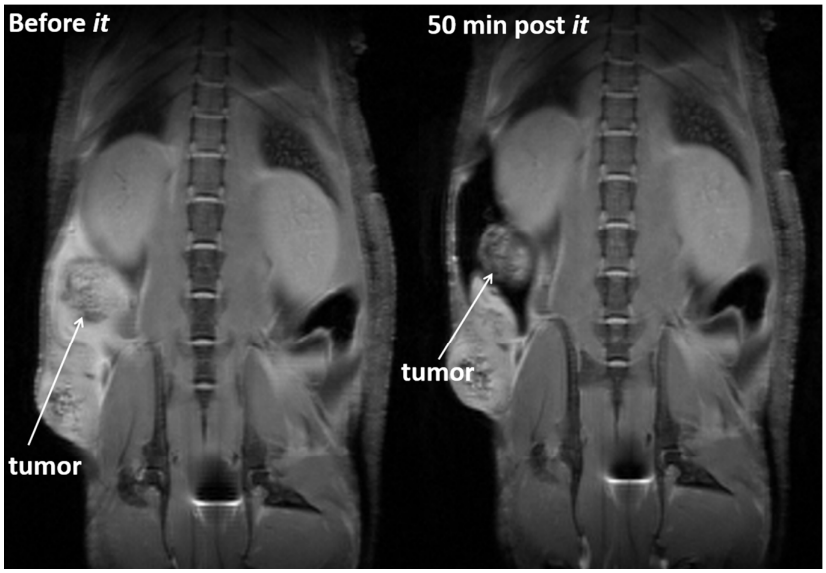

Figure 8: MRI images with turbo-rare spin-echo sequence (TR=2500, TE=12) of NPs10@D1_ICF_DOTAGA injected mouse at t = 0 (left) and t = 50 min (right) post intra-tumoral injection (*it*).

The biodistribution kinetics of NPs10@D1_DOTAGA have also been studied after intraperitoneal (*ip*) injection of 100 µL at 11.5 mM **(ESI, Figure S6)**. EHC values showed a maximum liver contrast of -60 % at 180 min post *ip* and very low contrast enhancement in tumor, muscles and bladder. On the other hand, EHC signal started increasing in kidneys at 150min post *ip*, indicating NPs' accumulation and a possible urinary excretion.

As expected, biodistribution kinetics are much slower after *ip* injection as shown by EHC values in bladder and liver. Thus, 180 min might not be a timescale long enough to assess the *in vivo* behavior of NPs10@D1_DOTAGA. Those *in vivo* MRI studies lean toward urinary and hepatobiliary excretions of both DPs although longer timescales have to be explored. The targeting probe NPs10@D1_ICF_DOTAGA presented low specific tumor uptake as a low EHC value of -20% maximum has been recorded.

In vivo planar scintigraphy studies and biodistribution from organs counting

For biodistribution studies using planar scintigraphy, dendritic probes NPs10@D1_ DOTAGA and NPs10@ D1_ICF_DOTAGA were labeled with Lutetium-177 radionuclide (half-life: 6.65 days). Optimization of radiolabeling conditions was performed by varying the temperature (from 45 to 90 °C) and the time (from 5 min to 3 h) while keeping pH at 6.0 by the use of

ammonium acetate 0.2 M buffer in order to avoid dendrimer-shell degradation of NPs. The highest reaction yield was obtained at 60 °C for 45 min leading after centrifugal purification by 50K molecular weight cut-off filters radiolabeled NPs in 68-78% overall radiochemical yields and radiochemical purities up to 96%.

In order to evaluate the ability of [^{177}Lu]Lu-NPs to target tumors *in vivo*, biodistribution studies were performed in B16F0 melanoma bearing nude mice at 30 min, 2 h, 6 h and 24 h post *iv* injection in the tail vein. Planar scintigraphy images are represented in **Figure 9** and show the biodistribution over time in mice injected with the radiolabeled control and melanoma-specific targeted NPs. 30min post *iv* injection of [^{177}Lu]Lu-NPs10@D1_DOTAGA high level of radioactivity were observed in liver (32,75 ± 4,71% ID/g), spleen (10,03 ± 4,22 %ID/g) and kidneys **(Figure 9, top)** with values of 1,51 ± 0,1 %ID/g. Highest tumor uptake could also be noticed at such short time delay post *iv* injection with values of 1,28 ± 0,16 %ID/g. At 24h *pi*, the radioactive signal decreased in liver and increased in lungs, emphasizing the NPs metabolization or degradation process over time. Regarding [^{177}Lu]Lu-NPs10@D1_ICF_DOTAGA, most of the radioactivity was observed in liver, spleen and kidneys at 30 min *pi* **(Figure 9, bottom)** however its lower biodistribution kinetics was evidenced by the highest radioactivity level in tumor at 6 h (3,43 ± 1,06 %ID/g) , whereas [^{177}Lu]Lu-NPs10@D1_DOTAGA was uptaken by the tumor after 30 min post *iv*. Renal excretion is evidenced by the increase of bladder radioactive signal at 6h *pi*.

For both radiolabeled agents, one must notice also skeleton signal due to free ^{177}Lu releasing thus evidencing *in vivo* transmetallation and/or transchelation phenomena a few hours post *iv*.

When considering the ratio of the mean values of tumour uptake /muscle uptake (T/M), higher values were obtained for [^{177}Lu]Lu-NPs10@D1_ICF_DOTAGA as compared to [^{177}Lu]Lu-NPs10@D1_DOTAGA, as a reflection of *in vivo* targeting.

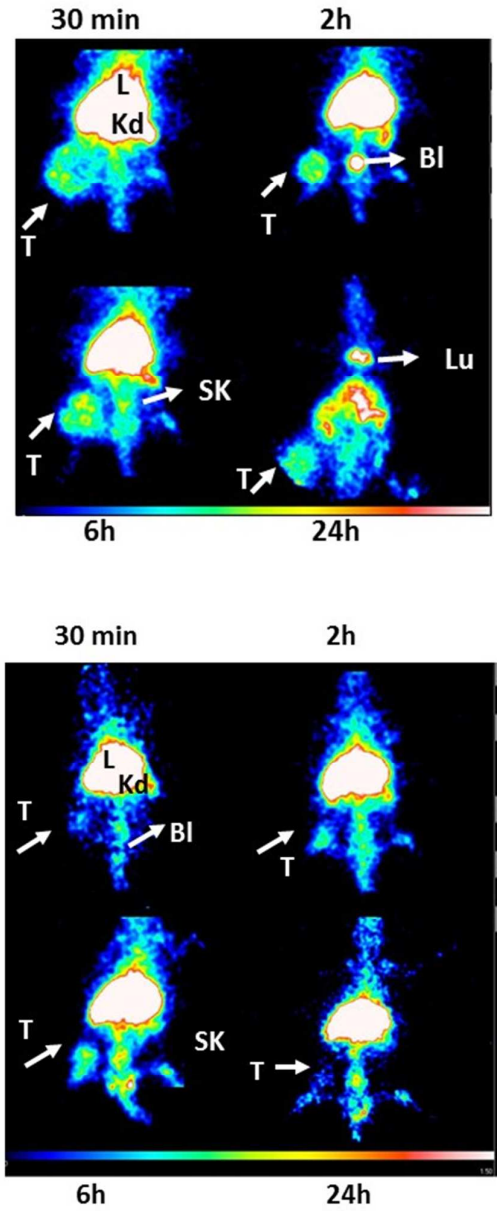

Figure 9: Planar scintigraphy images of mice injected with NPs10@D1_DOTAGA_177Lu (top) and [^{177}Lu]Lu-NPs10@D1_ICF_DOTAGA (bottom) at various times post *iv* injection. Bl = bladder; Kd = kidneys; L = liver; SK = skeleton; T = tumour.

Table 3: Distribution (percentage of injected dose per gram of tissue) of [^{177}Lu]Lu-NPs10@D1_DOTAGA in B16F0 bearing nude mice, from radioactive counting at 30 min, 2 h, 6 h and 24 h pi with 2 to 3 animals per time point except for 24 h time point (n = 1).

	30 min	sd	2h	sd	6h	sd	24h
Tumour	1.28	0.16	1.23	0.44	1.11	0.54	3.56
Eyes	0.21	0.04	0.15	0.11	0.06	0.03	0.05
Heart	1.32	0.01	0.78	0.49	0.38	0.34	0.29
Bladder	0.72	0.01	2.86	2.96	1.09	1.03	1.68
Spleen	10.03	4.22	7.26	3.97	4.55	2.41	6.15
Intestines	0.32	0.02	0.37	0.14	0.23	0.15	1.38
Lung	7.27	7.54	1.61	0.90	0.99	0.86	15.49
Bones	0.75	0.90	1.85	0.27	1.39	0.60	4.40
Liver	32.75	4.71	36.29	13.52	24.01	19.29	7.56
Muscle	0.42	0.03	0.22	0.17	0.26	0.31	0.09
Kidneys	1.51	0.07	1.15	0.40	1.04	0.51	2.04
Brain	0.10	0.03	0.09	0.04	0.04	0.04	0.08
Stomach	1.63	1.92	0.75	0.78	0.70	0.59	4.46
Skeleton	1.42	0.46	1.57	0.08	1.58	1.04	36.12
T/M	**3.04**		**5.71**		**4.22**		**41.42**

Table 4: Distribution (percentage of injected dose per gram of tissue) of [^{177}Lu]Lu-NPs10@D1_ICF_DOTAGA in B16F0 bearing nude mice, from radioactive counting at 30 min, 2 h, 6 h and 24 h pi, with 2 to 3 animals per time point

	30 min	sd	2h	sd	6h	sd	24h	sd
Tumour	2.18	0.20	3.43	1.06	2.41	0.30	2.54	0.06
Eyes	0.13	0.04	0.15	0.05	0.03	0.03	0.05	0.02
Heart	1.17	0.24	0.61	0.12	0.30	0.09	0.23	0.05
Spleen	11.21	2.57	7.39	2.86	6.91	1.81	6.34	5.34
Intestines	0.38	0.21	0.40	0.08	0.23	0.03	0.13	0.01
Bones	1.69	1.08	4.29	1.23	2.70	0.55	2.05	1.85
Liver	38.13	18.80	35.16	10.07	32.41	2.97	22.30	18.83

Muscle	0.34	0.21	0.36	0.18	0.13	0.08	0.21	0.13
Kidneys	1.52	0.05	1.75	0.43	1.75	0.29	1.28	0.00
Brain	0.09	0.01	0.05	0.02	0.10	0.08	0.39	0.48
Stomach	0.85	0.07	1.52	1.06	1.30	0.90	0.41	0.18
Skeleton	2.98	0.32	3.42	0.04	2.80	2.10	5.95	2.53
T/M	**6.33**		**9.51**		**18.42**		**12.24**	

Ex vivo confocal microscopy studies on Human samples

Confocal images of impregnated Melanoma samples with NPs10@D1 were acquired at 45 and 95 min post impregnation. A low fluorescence signal was observed at both times, whereas EVCM mosaics of melanoma sample impregnated with NPs10@D1_ICF_ Alexa647_DOTAGA for 25 min **(ESI, Figure S7)** showed a moderate fluorescence co-localized with melanocytes.

Furthermore, additional studies have been performed at longer impregnation time (75 min) with NPs10@D1_ ICF_ Alexa647_DOTAGA **(Figure 10)** and in this case, EVCM showed a very high fluorescence signal of tumor cells at 658 nm that did not involve the surrounding epidermis and dermis. Co-localization of melanoma cells visible in the EVCM images acquired in the reflectance mode with the ICF-labelled dendronized NPs fluorescence indicated that this staining is specific for these cells.

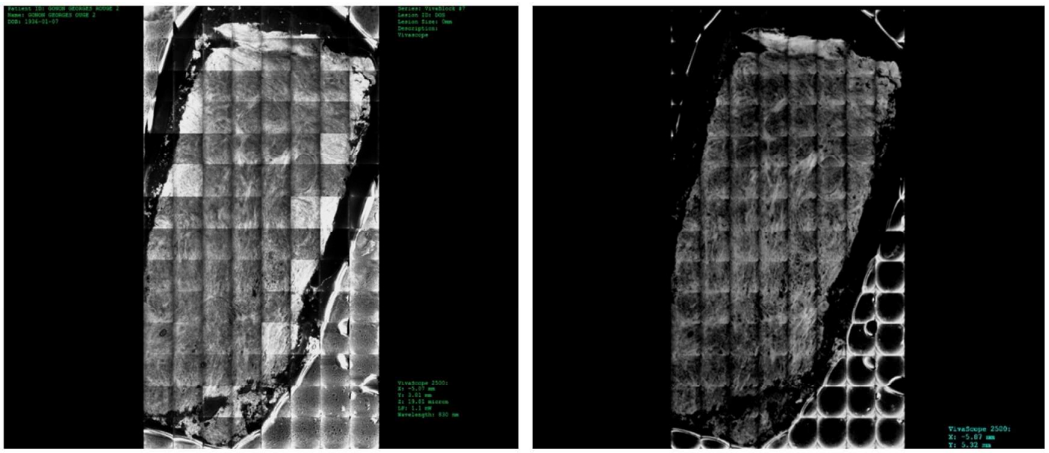

Figure 10: EVCM image of a melanoma sample at 75 min impregnation with NPs10@D1_ ICF_ Alexa647_ DOTAGA in the reflectance mode (Left) and in the fluorescence mode (Right).

4. Conclusion

The biodistribution of NPs10@D1_DOTAGA and melanin-targeting NPs10@D1_ICF_DOTAGA was studied *in vivo* using MRI and planar scintigraphy through ^{177}Lu-radiolabeling. MRI experiments showed high contrast power of both dendronized NPs and hepatobiliary and urinary excretions. Little tumor uptake could be observed probably as a consequence of the negatively charged DOTAGA-derivatized shell which reduces the diffusion across the cells' membrane. Planar scintigraphy images demonstrated a moderate specific tumor uptake of melanoma-targeted [^{177}Lu]Lu-NPs at 24 h post iv injection, with a tumor over muscle ratio (TMR) of 2.89 ± 1.2, and the highest tumor uptake of the control probe at 30 min *pi*, probably due to the EPR effect. In addition, EVCM studies showed a high specific targeting of human Melanoma samples impregnated with NPs10@D1_ICF_Alexa647_ DOTAGA. In the clinical practice, *in vivo* confocal microscopy and EVCM are mainly used in the reflectance mode for the diagnosis of Melanoma because melanin offers a natural contrast in this mode and no specific staining has been found for melanocytes. However, in the reflectance mode malignant melanocytes can show a similar morphology and reflectance to Langerhans cells with frequent misdiagnosis of Melanoma.[30]

The identification of melanocytes with NPs10@D1_ ICF_ Alexa647_ DOTAGA is of paramount importance for the diagnosis of Melanoma because the use of a specific marker for melanocytes can dramatically increase the diagnostic accuracy of confocal microscopy. Our study demonstrated that this marker can identify melanocytes in *ex vivo* conditions. Further studies should be performed in order to evaluate the potential use of this marker with *in vivo* fluorescence confocal microscopy directly on patients. Further EVCM studies on human samples are scheduled on over-expressing Melanin and a-Melanin Melanomas, as well as on basal cell Carcinoma and Naevus. These studies will assess the ability of ICF-labelled dendronized NPs to accurately identify cancerous from normal tissues and to diagnose efficiently and rapidly Melanoma.

Author contributions

The manuscript was written through the contributions of all authors. All authors have given approval to the final version of the manuscript.

Declaration of interest

The authors declare no conflict of interest.

Supporting Information

Figures S1-S7

Acknowledgements

The Région Alsace, France, and the University of Mons, Belgium, are gratefully acknowledged for the doctoral fellowship to Catalina Bordeianu. A. Parat, S. Begin-Colin and D. Felder-Flesch thank the Centre National de la Recherche Scientifique (CNRS) for the financial support on A. Parat post-doctoral research position via the DENDRIDIAG project. This research project was also co-funded by the European Regional Development Fund (ERDF) in the framework of the INTERREG V Upper Rhine program, "Transcending borders with every project", project NANOTRANSMED. Emilie Voirin, Emilie Couzigné, Céline Kieffer are gratefully acknowledged for their technical support and help in the everyday life of the laboratory.

This work was also performed with the support of the Fonds National pour la Recherche Scientifique (F.R.S.-FNRS), FEDER, the Walloon Region, the COST Actions, the Centre for Microscopy and Molecular Imaging (CMMI), supported by the European Regional Development Fund of the Walloon Region, and the ARC and UIAP programs.

Guilhem Pagès (UR370 QuaPA, INRA), and Carine Chassain (CHU Clermont-Ferrand, MRI department) from the Agroresonance Platform are gratefully acknowledged.

Notes and references

‡ The manuscript was written through contributions of all authors. All authors have given approval to the final version of the manuscript.

§ Conflict of interest: none.

References

[1] R. L. Siegel, K. D. Miller and A. Jemal, Cancer Statistics 2016, CA. Cancer J. Clin. 66(1) (2016) 7-30.

[2] National Cancer Institute, www.cancer.gov

[3] N. Kamaly, Z. Xiao, P. M. Valencia, A. F. Radovic-Moreno, O. C. Farokhzad, Targeted polymeric therapeutic nanoparticles: design, development and clinical translation, Chem. Soc. Rev. 41(7) (2012) 2971–3010.

[4] J. E. Rosen, L. Chan, D.-B. Shieh, F. X. Gu, Iron oxide nanoparticles for targeted cancer imaging and diagnostics., Nanomedicine 8(3) (2012) 275-90.

[5] T. M. Allen, Ligand-targeted therapeutics in anticancer therapy., Nat. Rev. Cancer 2(10) (2002) 750-763.

[6] a) N. Bertrand, J. Wu, X. Xu, N. Kamaly, O. C. Farokhzad, Cancer nanotechnology: the impact of passive and active targeting in the era of modern cancer biology, Adv. Drug Deliv. Rev. 66 (2014) 2-25.

[7] C. S. Kue, A. Kamkaew, K. Burgess, L. V. Kiew, L. Y. Chung, H. B. Lee, Small molecules for active targeting incancer, Med. Res. Rev. 36(3) (2016) 494-575.

[8] Melanoma, *Nature Outlook* 515(7527) (2014).

[9] E. C. Borden, Melanoma: biologically targeted therapeutics, Human Press, 2002.

[10] F. O. Smith, S. G. Downey, J. A. Klapper, J. C.Yang, R. M. Sherry, R. E. Royal, U. S. Kammula, M. S. Hughes, N. P. Restifo, C. L. Levy, D. E.White, S. M. Steinberg, S. A. Rosenberg, Treatment of metastatic melanoma using Interleukin-2 alone or in conjunction with vaccines, *Clin. Cancer Res.* 14(17) (2008) 5610-5618.

[11] G. Jiang, R. H. Li, C. Sun, Y. Q. Liu, J. N. Zheng, Dacarbazine combined targeted therapy versus dacarbazine alone in patients with malignant melanoma: A meta-analysis, PLoS One 9(12) (2014) 1-13.

[12] S. P. Patel, S. E. Woodman, Profile of ipilimumab and its role in the treatment of metastatic Melanoma, Drug Des. Devel. Ther. 5 (2011) 489-495.

[13] P. B. Chapman, A. Hauschild, C. Robert, J. B. Haanen, P. Ascierto, J. Larkin, R. Dummer, C. Garbe, A. Testori, M. Maio, D. Hogg, P. Lorigan, C. Lebbe, T. Jouary, D. Schadendorf, A. Ribas, S. J. O'Day, J. A. Sosman, J. M. Kirkwood, A. M. M. Eggermont, B. Dreno, K. Nolop, J. Li, B. Nelson, J. Hou, R. J. Lee, K.

T. Flaherty, G. A. McArthur, Improved survival with vemurafenib in melanoma with BRAF V600E mutation., N. Engl. J. Med. 364(26) (2011) 2507-2516.

[14] F. Degoul, M. Borel, N. Jacquemot, S. Besse, Y. Communal, F. Mishellany, J. Papon, F. Penault-Llorca, D. Donnarieix, M. Doly, L. Maigne, E. Miot-Noirault, A. Cayre, J. Cluzel, N. Moins, J. M. Chezal, M. Bonnet, In vivo efficacy of melanoma internal radionuclide therapy with a 131I-labelled melanin-targeting heteroarylcarboxamide molecule, Int. J. Cancer 133(5) (2013) 1042-1053.

[15] J. Molieras, J. M. Chezal, E. Miot-Noirault, A. Roux, L. Heinrich-Balard, R. Cohen, S. Tarrit, C. Truillet, A. Mignot, R. Hachani, D. Kryza, R. Antoine, P. Dugourd, P. Perriat, M. Janier, L. Sancey, F. Lux, O. Tillement, Development of gadolinium based nanoparticles having an affinity towards melanin, Nanoscale 5 (2013) 1603-1623.

[16] a) F. Cachin, E. Miot-Noirault, B. Gillet, V. Isnardi, B. Labeille, P. Payoux, N. Meyer, S. Cammilleri, C. Gaudy, M. Razzouk-Cadet, J. P. Lacour, F. Granel-Brocard, C. Tychyj, F. Benbouzid, J. D. Grange, F. Baulieu, A. Kelly, C. Merlin, D. Mestas, F. Gachon, J. M. Chezal, F. Degoul, and M. D'Incan, 123I-BZA2 as a Melanin-Targeted Radiotracer for the Identification of Melanoma Metastases: Results and Perspectives of a Multicenter Phase III Clinical Trial. J. Nucl. Med. 55 (2014) 15-22.

[17] P. Auzeloux, J. Papon, E. M. Azim, M. Borel, R. Pasqualini, A. Veyre, and J. C. Madelmont, A potential melanoma tracer: Synthesis, radiolabeling, and biodistribution in mice of a new nitridotechnetium bis(aminothiol) derivative pharmacomodulated by a N-(diethylaminoethyl)benzamide, J. Med. Chem. 43(2) (2000) 190-198.

[18] J. M. Chezal, J. Papon, P. Labarre, C. Lartigue, M. J. Galmier, C. Decombat, O. Chavignon, J. Maublant, J. C. Teulade, J. C. Madelmont, and N. Moins, Evaluation of radiolabeled (Hetero)aromatic analogues of N-(2-diethylaminoethyl)-4-iodobenzamide for imaging and targeted radionuclide therapy of melanoma, J. Med. Chem. 51(11) (2008) 3133-3144.

[19] P. Labarre, J. Papon, M.-F. Moreau, N. Moins, M. Bayle, A. Veyre, and J.-C. Madelmont, Melanin affinity of N-(2-diethylaminoethyl)-4-iodobenzamide, an effective melanoma imaging agent, Melanoma Reseach 12(2) (2002) 115-121.

[20] A. Parat, D. Kryza, F. Degoul, J. Taleb, C. Viallard, M. Janier, A. Garofalo, P. Bonazza, L. Heinrich-Balard, R. Cohen, E. Miot-Noirault, J.-M. Chezal, C. Billotey, and D. Felder-Flesch, Radiolabeled dendritic probes as tools for high in vivo tumor targeting: application to melanoma, J. Mater. Chem. B 3(12) (2015) 2560-2571.

[21] B. Basly, G. Popa, S. Fleutot, B. Pichon, A. Garofalo, C. Ghobril, C. Billotey, A. Berniard, P. Bonazza, H. Martinez, P. Perriat, D. Felder-Flesch, and S. Begin-Colin, Influence of the nanoparticle

synthesis way on dendronized iron oxides as MRI contrast agents, Dalton Trans. 42 (2013) 2146-2156.

[22] F. Meyer, M. Dimitrova, J. Jedrzejenska, Y. Arntz, P. Schaaf, B. Frisch, J.-C. Voegel, and J. Ogier, Relevance of bi-functionalized polyelectrolyte multilayers for cell transfection, Biomaterials 29(5) (2008) 618-624.

[23] $^{177}LuCl_3$/ 0.05N HCl -Perkin Elmer, specific activity > 740 GBq/mg.

[24] ITLC- Instant Thin Layer Chromatography.

[25] E. Miot-Noirault, A. Vidal, J. Morlieras, P. Bonazza, P. Auzeloux, S. Besse, M.-M. Dauplat, C. Peyrode, F. Degoul, C. Billotey, F. Lux, F. Rédini, O. Tillement, J.-M. Chezal, D. Kryza, and M. Janier, Small rigid platforms functionalization with quaternary ammonium: Targeting extracellular matrix of chondrosarcoma, Nanomedicine: Nanotechnology, Biology and Medicine 10(8) (2014) 1887-1895.

[26] A. Garofalo, A. Parat, C. Bordeianu, C. Ghobril, M. Kueny-Stotz, A. Walter, J. Jouhannaud, S. Begin-Colin, D. Felder-Flesch, Efficient synthesis of small-sized phosphonated dendrons:potential organic coatings of metal oxide nanoparticles, New J. Chem. 38 (2014) 5226-5239.

[27] C. Ghobril and G. Popa, C. Billotey, P. Bonazza, J. Taleb, S. Begin-Colin, D. Felder-Flesch, Bisphosphonate tweezer and clickable PEGylated PAMAM dendrons for the elaboration of functional iron oxide nanoparticles displaying renal and hepatobiliary eliminations, Chem. Commun. 49 (2013) 9158-9160.

[28] A. Walter, A. Parat, A. Garofalo, S. Laurent, L. Vander Elst, R. N. Muller, T. Wu, E. Heuillard, E. Robinet, F. Meyer, D. Felder-Flesch, S. Begin-Colin, Modulation of relaxivity, suspension stability and biodistribution of dendronized iron oxide nanoparticles as a function of the organic shell design, Part. Part. Syst. Charact. 32(5) (2015) 552-560.

[29] CheMatech, Usual Chemical Name NH2-DOTA-GA and CAS Number: 306776-79-4.

[30] P. Hashemi, M. P. Pulitzer, A. Scope, I. Kovalyshyn, A. C. Halpern, A. A. Marghoob, J. Am. Acad. Dermatol. 66(3) (2012) 452-462.

Graphical Abstract